Asian Journal of Chemistry; Vol. 37, No. 11 (2025), 2725-2732
ASIAN JOURNAL OF CHEMISTRY
https://doi.org/10.14233/ajchem.2025.34579

Hydrothermal Synthesis and Characterization of $Fe_2(MoO_4)_3$/*g*-C_3N_4 Composites for Improved Energy Storage Applications

V. SUBAPRIYA[1,2,*], M. GOWTHAM[3], D. KARTHICKEYAN[4], R. JANANI[5] and K. VENKATACHALAM[2]

[1]Department of Physics, Government College of Technology, Coimbatore-641013, India
[2]Department of Physics, Government Arts College (Autonomous), Coimbatore-641018, India
[3]PG and Research and Department of Physics, Kongunadu Arts and Science College, Coimbatore-641029, India
[4]Department of Physics, Government College of Engineering Srirangam, Trichirappalli-620012, India
[5]Department of Physics, KIT-Kalaignarkarunanithi Institute of Technology, Coimbatore-641018, India

*Corresponding author: E-mail: subapriya.physics@gct.ac.in

Received: 1 August 2025 *Accepted*: 13 September 2025 *Published online*: 27 October 2025 AJC-22159

In this study, pristine $Fe_2(MoO_4)_3$ and its composite with *g*-C_3N_4 were synthesized *via* a hydrothermal approach. The resultant crystal structure was verified through X-ray diffraction, while energy dispersive spectroscopy and field emission scanning electron microscopy were utilized to determine elemental composition and sample morphology, respectively. Fourier transform infrared spectroscopy further affirmed the successful preparation of the target materials. Both pure and composite samples underwent photo-electrochemical evaluation, revealing that $Fe_2(MoO_4)_3$ combined with 2 g of *g*-C_3N_4 exhibited a remarkable specific capacitance of 1157.16 F g^{-1} and retained 99.70% of its capacitance after 2500 cycles, demonstrating exceptional electrochemical stability.

Keywords: Molybdenum, Iron, *g*-C_3N_4, Supercapacitor, Hydrothermal method.

INTRODUCTION

Supercapacitors possess unique operational features such as ultra-fast charging/discharging, high power density and excellent cyclability, making them ideal for electric transport, portable electronics and large-scale energy storage [1,2]. These attributes largely depend on the design and selection of electrode materials, whose physico-chemical and microstructural properties influence capacitance, rate performance and stability [3]. Current research highlights that rational electrode engineering such as nanoscale structuring or hybridization with conductive polymers can enhance ion/electron transport and surface area, boosting device performance. Molybdenum ions, exhibiting oxidation states from +6 to 0, offer exceptional electrochemical properties and high specific capacitance. As a result, metal molybdates like $CoMoO_4$, $NiMoO_4$ and $MnMoO_4$ are considered promising supercapacitor electrode materials. When Mo combines with transition metals, it forms stable oxides, with Mo typically existing as an oxyanion ($[MoO_4]^{2-}$), contributing abundant redox-active sites [4-8].

To enhance the inherent catalytic activity, iron is commonly used as a dopant. However, increasing evidence suggests that iron atoms serve as the primary active sites during the oxygen evolution reaction process. Consequently, researchers have explored the electrolytic properties of $Fe_2(MoO_4)_3$ to better understand and leverage its performance. Among these, orthorhombic $Fe_2(MoO_4)_3$ emerges as a highly promising material due to its exceptional performance [9-11]. Moreover, *g*-C_3N_4, a polymeric 2D semiconductor, is recognized as a promising catalyst because of its simple synthesis process, low cost, lightweight nature, excellent biocompatibility, unique electronic structure and high stability. Its electrocatalytic performance significantly improves when combined with efficient co-catalysts such as graphene oxide, carbon nanotubes (CNTs) or metal oxides [12-14]. Various advanced modification techniques, such as morphological tuning, functional group modifications, elemental doping, defect engineering and the construction of homo and heterojunctions, have been proposed to overcome these inherent limitations. Among the promising materials, molybdenum trioxide (MoO_3) [15] and iron(III) molybdate ($Fe_2(MoO_4)_3$) [16] have emerged as prominent n-type semiconductors with narrow energy band gaps. These materials are abundant, highly stable, cost-effective and environmentally sustainable.

This study investigates the hydrothermal synthesis of $Fe_2(MoO_4)_3$:*g*-C_3N_4 composites and systematically evaluates their effectiveness as electrode materials for advanced supercapacitors. When these engineered composites are deposited onto nickel foam substrates, they demonstrate remarkable specific capacitance and cycling stability. Such performance underscores their significant potential as pseudocapacitive materials in energy storage applications. The enhancement in the electrochemical activity can be attributed to the synergistic effects between $Fe_2(MoO_4)_3$ and the 2D structure of *g*-C_3N_4, which facilitates ion diffusion and rapid electron transport, promoting high-rate capability and robust durability during the charge-discharge operations. These findings align with recent literature emphasizing the critical importance of nanostructured electrode design and composite engineering to achieve superior supercapacitor performance.

EXPERIMENTAL

All reagents were of analytical grade and used as received without further purification. Melamine (≥ 99%, Merck) was employed as the precursor for *g*-C_3N_4. Ferric nitrate nonahydrate ($Fe(NO_3)_3{\cdot}9H_2O$), SRL Chemicals), ammonium heptamolybdate tetrahydrate ($(NH_4)_6Mo_7O_{24}{\cdot}4H_2O$, Hi-Media), and citric acid ($C_6H_8O_7$, Merck) served as starting materials for the $Fe_e(MoO_4)_3$ framework. Ethanol (99.9%) and deionized water (18.2 MΩ cm) were used for washing and dispersion. Potassium hydroxide (1 M) was used as the electrolyte in all electrochemical measurements.

The structure of synthesized powders was identified by X-ray diffraction pattern (XRD) using Cu*K*α radiation (λ = 1.5417 Å) on a PANalytical X'Pert PRO diffractometer operated at 40 kV and 30 mA. Field-emission scanning electron microscopy (FESEM, FEI-QUANTA-FEG 250) equipped with energy-dispersive X-ray spectroscopy (EDS) provided surface morphology and elemental composition. Fourier-transform infrared (FTIR) spectra were recorded in the 4000–400 cm^{-1} region using a Perkin-Elmer Spectrum Two spectrometer. The electrochemical measurements (CV, GCD, EIS) were performed at room temperature on a CHI660E electrochemical workstation (CH Instruments, USA) using a three-electrode configuration.

Preparation of *g*-C_3N_4: To prepare *g*-C_3N_4, a thermal polymerization process was conducted using melamine as the precursor material. Melamine (10 g) were loaded into a 250 mL alumina crucible, then heated in a muffle furnace with the temperature ramped at 5 ºC/min until reaching 450 ºC. The sample was maintained at this temperature for 3 h to facilitate complete condensation. After cooling to ambient temperature, the obtained yellow product was carefully collected and finely milled to yield powdered *g*-C_3N_4.

Preparation of Fe_2MoO_4: A mixture of ferric nitrate (8.484 g), ammonium heptamolybdate (3.707 g), citric acid (0.4208 g) was thoroughly dissolved in 80 mL deionized (DI) water followed by continuous stirring for 1 h to ensure complete homogenization. The precursor mixture was transferred to a sealed autoclave and subjected to a hydrothermal process at 180 ºC for 24 h, with a controlled heating rate of 5 ºC per min to ensure gradual temperature increase and uniform nucleation. Upon completion of hydrothermal treatment, the resulting product was separated by filtration and sequentially washed with ethanol and deionized water to eliminate impurities. The collected solid was then dried at 60 ºC for 24 h to remove residual moisture, followed by an annealing step at 450 ºC for 3 h to enhance crystallinity and phase purity.

Preparation of Fe_2MoO_4/*g*-C_3N_4: Different portions of *g*-C_3N_4 1 g, 1.5 g and 2 g were added to separate 100 mL beakers containing 40 mL deionized water under 1 h of sonication. A solution was made by mixing 4.242 g of ferric nitrate, 1.853 g of ammonium heptamolybdate and 0.2101 g of citric acid in 40 mL of DI water for each *g*-C_3N_4 ratio. The *g*-C_3N_4 dispersions to each solution that was being dropwise added. The stainless-steel autoclaves received the prepared mixtures which underwent heating at 180 ºC for 24 h while using a heating rate of 5 ºC per min. The products underwent filtration until complete drying at 60 ºC for 24 h after being washed with deionized water and ethanol. Three different dopant concentration experienced a 3 h annealing process at 450 ºC as the last step.

Electrode preparation: For conductance testing the three-electrode configuration was used to analyze pure $Fe_2(MoO_4)_3$ together with $Fe_2(MoO_4)_3$:*g*-C_3N_4. $Fe_2(MoO_4)_3$:*g*-C_3N_4 operated as working electrode and a reference electrode belonged to Ag/AgCl with a platinum wire operated as counter electrode. The working electrode synthesized by mixing 0.7 mg of $Fe_2(MoO_4)_3$:*g*-C_3N_4 together with 0.2 mg of activated carbon and 0.1 mg of polytetrafluoroethylene followed by adding few drops of ethanol to create the slurry. The slurry was uniformly coated on nickel foam sheet of 1 cm^2 which underwent drying at 70 ºC for 4 h. A 1 M KOH solution acts as an electrolytic solution. The measurements for specific capacitance together with energy density relied on an active material.

RESULTS AND DISCUSSION

Structural and morphological studies: The crystalline structure and phase composition of the synthesized samples were systematically analyzed *via* XRD, while FESEM was employed to closely examine their surface features and microstructural morphology. The crystallinity of the synthesized $Fe_2(MoO_4)_3$:*g*-C_3N_4 (1, 1.5 and 2 g) was evaluated using XRD presented in Fig. 1. It was revealed that the pristine $Fe_2(MoO_4)_3$ exhibit the characteristic peaks identified at 22.70º, 25.74º, 26.63º, 27.71º, 30.86º, 32.03º, 34.20º, 35.86º, 38.1º, 39.41º, 40.88º, 43.54º, 45.79º, 49.13º, 53.17º, 57.19º, 60.17º, 62.61º, 66.54º and 68.99º, corresponding to the (310), (212), (400), (411), (113), (322), (132), (004), (422), (332), (233), (224), (414), (125), (542), (344), (551), (733) and (461) planes, respectively. These peaks confirm $Fe_2(MoO_4)_3$ with an orthorhombic structure and *Pbcn* space group. The peak at 27.4º represents the characteristic peak of *g*-C_3N_4 [17]. The observed peaks of pristine $Fe_2(MoO_4)_3$ correspond to JCPDS card 01-085-2287 and *g*-C_3N_4 exhibit peaks corresponding to JCPDS card no. 87-1526. However, the intensity of $Fe_2(MoO_4)_3$:*g*-C_3N_4 diffraction peaks significantly increase when adding *g*-C_3N_4. These XRD data confirm the effective synthesis of both pure $Fe_2(MoO_4)_3$ and $Fe_2(MoO_4)_3$:*g*-C_3N_4.

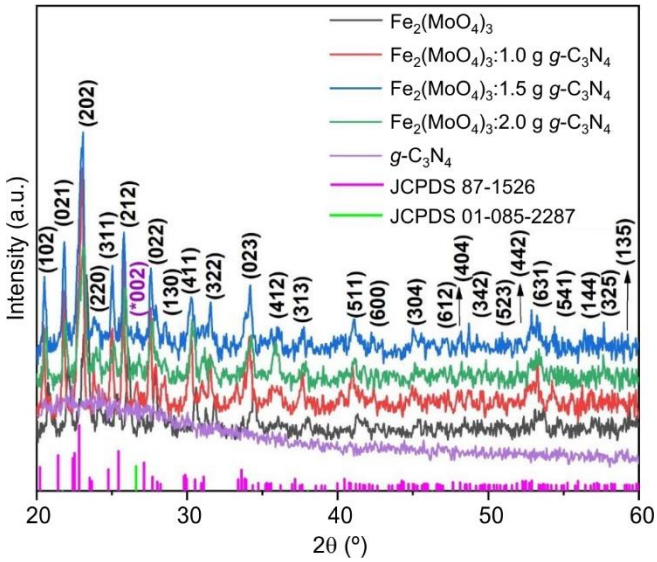

Fig. 1. XRD spectra of pristine $Fe_2(MoO_4)_3$ and $Fe_2(MoO_4)_3$:g-C_3N_4 (1.0, 1.5 and 2 g)

Morphological studies: FESEM was employed to analyze the morphologies of the synthesized pristine $Fe_2(MoO_4)_3$ as well as $Fe_2(MoO_4)_3$ composites incorporating various amounts (1.0, 1.5 and 2.0 g) of g-C_3N_4. Fig. 2a showed the characteristic of pure $FeMoO_4$ as a 2D spherical shape likely with some degree of agglomeration [18]. Fig. 2b-d showed that $FeMoO_4$ nano-particles was dispersed in g-C_3N_4 nanosheets and confirmed that strong interface formed between $Fe_2(MoO_4)_3$ and g-C_3N_4, which was conductive to transfer of electrons and enhancing its super capacitive performance when increasing the g-C_3N_4 content.

Fig. 3a shows that Fe, Mo and O elements are visible in the EDS spectrum when the element is pristine $Fe_2(MoO_4)_3$ and Fig. 3b-d shows that Fe, Mo, O, C and N are visible when the element is $Fe_2(MoO_4)_3$:g-C_3N_4. No other traces of elements were detected in the EDS peaks, confirming that the intended composition of the produced nanoparticles. Table-1 displays the findings of the quantitative investigation, which include the K ratio, atomic percentage and $Fe_2(MoO_4)_3$:g-C_3N_4. There is no doubt that these nanoparticles densely consisted of g-C_3N_4.

FTIR studies: As depicted in Fig. 4, the FTIR spectra of pure $Fe_2(MoO_4)_3$ and $Fe_2(MoO_4)_3$ composites incorporating increasing amounts of g-C_3N_4 (1, 1.5 and 2 g) provide comprehensive insight into the chemical structure and phase composition of the synthesized materials. The broad absorption centered within the 1750-1600 cm^{-1} range, once deconvoluted, yields peaks at 1709, 1678 and 1076 cm^{-1}, all of which correspond to stretching vibrations of the oxalate C=O functional group. Such assignments agree with FTIR analyses commonly reported for metal oxide-carbon composites. The presence of a prominent 1624 cm^{-1} band is indicative of water bending modes, underscoring the hydration or environmental water content typical in these systems. The 1316 cm^{-1} feature

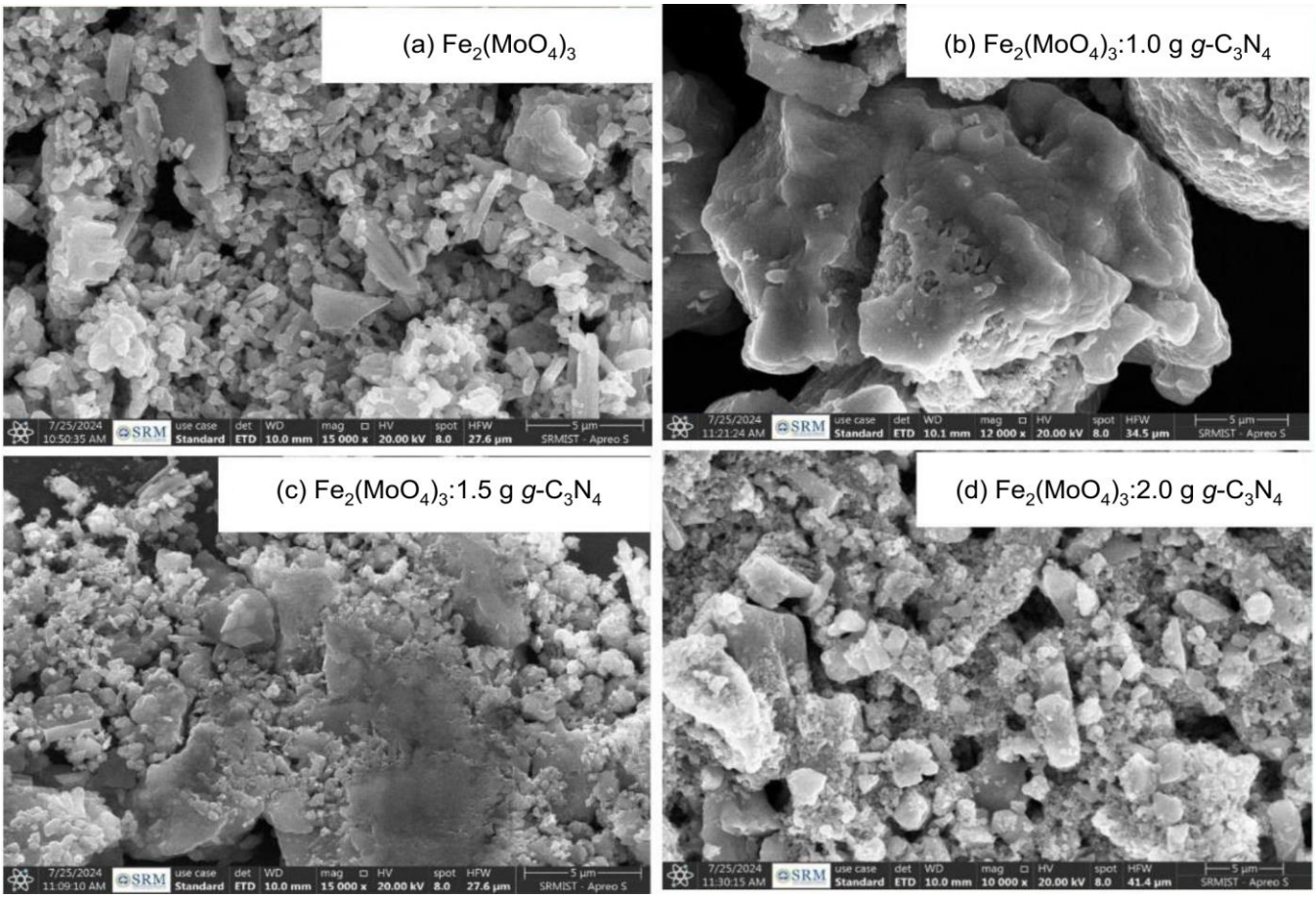

Fig. 2. FESEM images of pristine $Fe_2(MoO_4)_3$ and $Fe_2(MoO_4)_3$:g-C_3N_4 (1.0, 1.5 and 2.0 g)

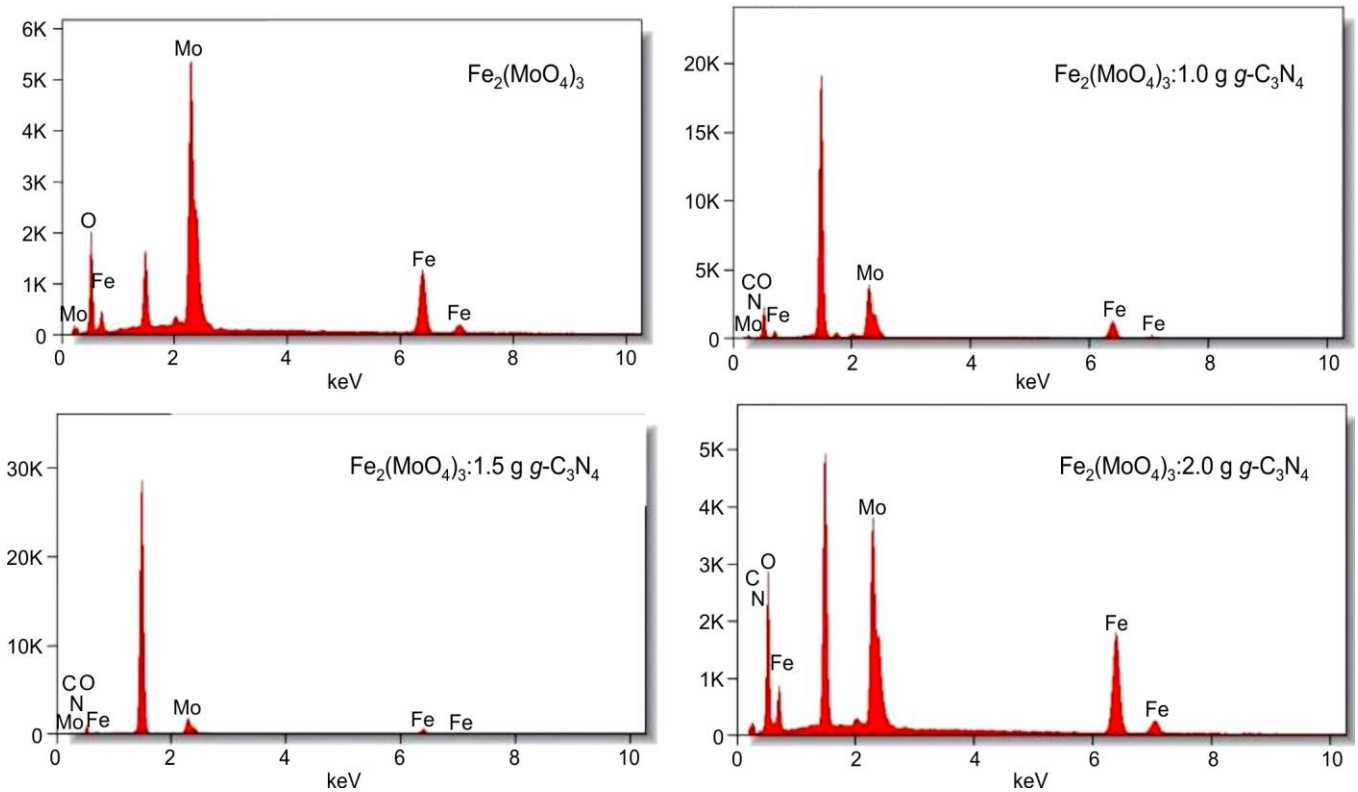

Fig. 3. EDS images of pristine $Fe_2(MoO_4)_3$ and $Fe_2(MoO_4)_3$:*g*-C_3N_4 (1, 1.5 and 2 g)

TABLE-1
EDS SPECTRA OF $Fe_2(MoO_4)_3$ AND $Fe_2(MoO_4)_3$:*g*-C_3N_4

(a) $Fe_2(MoO_4)_3$			(b) $Fe_2(MoO_4)_3$:1 g *g*-C_3N_4		
Element	Weight (%)	Atom (%)	Element	Weight (%)	Atom (%)
O K	32.99	70.79	C K	1	2.49
Fe K	20.39	12.54	N K	2	4.26
Mo L	46.62	16.4	Fe K	30.18	16.11
Total	100		Mo L	32.96	10.25
			O K	35.86	33.86
			Total	100	
(c) $Fe_2(MoO_4)_3$:1.5 g *g*-C_3N_4			(d) $Fe_2(MoO_4)_3$:2 g *g*-C_3N_4		
Element	Weight (%)	Atom (%)	Element	Weight (%)	Atom (%)
C K	1.12	2.72	C K	2.82	6.61
N K	3	6.25	N K	4	8.04
Fe K	30.18	15.78	Fe K	23.25	11.72
Mo L	32.66	10.03	Mo L	37.52	11.3
O K	33.04	65.22	O K	32.41	62.33
Total	100		Total	100	

is related to combined C–O and OCO vibrational modes, reflecting the complex interplay of organic moieties in the microstructure of samples. The Mo=O stretching vibrations, apparent at 955 and 914 cm^{-1}, highlight the inclusion of hydrated oxalate complexes, while the 817 cm^{-1} absorption is attributed to tetrahedral Mo(VI)–O configurations. The well-defined band at 556 cm^{-1} is characteristic of Fe(III)–O octahedral coordination, corroborating previous findings for crystalline Fe-molybdate and its hybrid derivatives [19-22]. The sharp-ness of these bands signals a well-ordered, crystalline state for the $Fe_2(MoO_4)_3$ matrix. Moreover, the positions of the $Fe_2(MoO_4)_3$ specific peaks are consistently retained across samples with added *g*-C_3N_4, with only minimal shifts observed, implying a structural compatibility and successful integration of *g*-C_3N_4 without significant disruption of the parent crystal lattice. Such subtle wavenumber adjustments are likely a result of interfacial interactions between the $Fe_2(MoO_4)_3$ framework and the incorporated *g*-C_3N_4.

Electrochemical performance

Cyclic voltammetry (CV) measurements: Following the activation procedure, multiple cyclic voltammetry (CV) cycles were carried out to evaluate the electrochemical characteristics and ensure the stabilization of the electrode response,

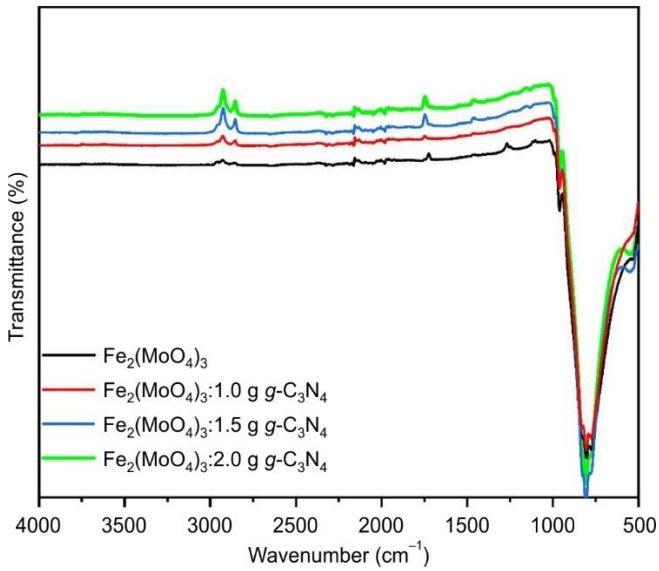

Fig. 4. FTIR spectra of pristine $Fe_2(MoO_4)_3$ and $Fe_2(MoO_4)_3$:g-C_3N_4 (1.0, 1.5 and 2.0 g)

a practice commonly employed to verify the reproducibility and readiness of supercapacitor electrodes for subsequent electrochemical testing. The cyclic voltammetry responses shown in Fig. 5a-e compare the electrochemical behaviour of pure $Fe_2(MoO_4)_3$ with that of $Fe_2(MoO_4)_3$ electrodes modified through the incorporation of 1, 1.5 and 2 g of g-C_3N_4.

These measurements were conducted within a voltage range of –0.2 to 0.3 V at ambient temperature, employing scan rates from 10 to 100 mV/s. Notably, as observed in Fig. 5a, the anodic and cathodic currents increase as scan rate rises, substantiating a positive correlation between scan velocity and capacitive current that is characteristic of pseudocapacitive charge storage processes. This behaviour is indicative of well-designed nanostructured electrodes, where the presence of g-C_3N_4 facilitates faster electron and ion transport, subsequently boosting the rate capability and overall electrochemical performance [6]. The CV curves exhibit salient redox peaks typical of $Fe_2(MoO_4)_3$ systems and their stable, repeatable profiles affirm strong electrochemical durability of the electrodes. Deviation from the ideal rectangular shape is observed in the CV signatures, primarily due to the oxygen-containing functional groups on the electrode surface and their redox activity, which is characteristic for pseudocapacitive materials and similar to phenomena described for g-C_3N_4 integrated hybrids [4,5]. Moreover, all samples display pronounced negative redox peaks near 0.15 V, associated with oxygen evolution processes, where enhanced current density, oxygen release and peak shifts become more evident at higher scan rates, a behaviour attributed to increased electrode resistance and charge transfer limitations [6,23]. For $Fe_2(MoO_4)_3$:g-C_3N_4 composites, increasing g-C_3N_4 concentration (1-2 g) results in expanded CV enclosed areas, which translates directly into improved capacitive energy storage potential. The composite electrodes demonstrate related to the pseudocapacitive features, with all samples exhibiting non-rectangular CV curves that affirm dominant role of $Fe_2(MoO_4)_3$ in charge storage, while minor peak shifts further indicate the presence of series and contact resistance in the hybrid electrode system [4,6,23]. The enhanced electrochemical response is further facilitated by the porous morphology of g-C_3N_4, which supports efficient electrolyte infiltration and improved charge transfer, thus augmenting overall performance [5,11,12].

Cyclic stability measurements: The values for specific capacitance and retention were obtained by conducting cyclic

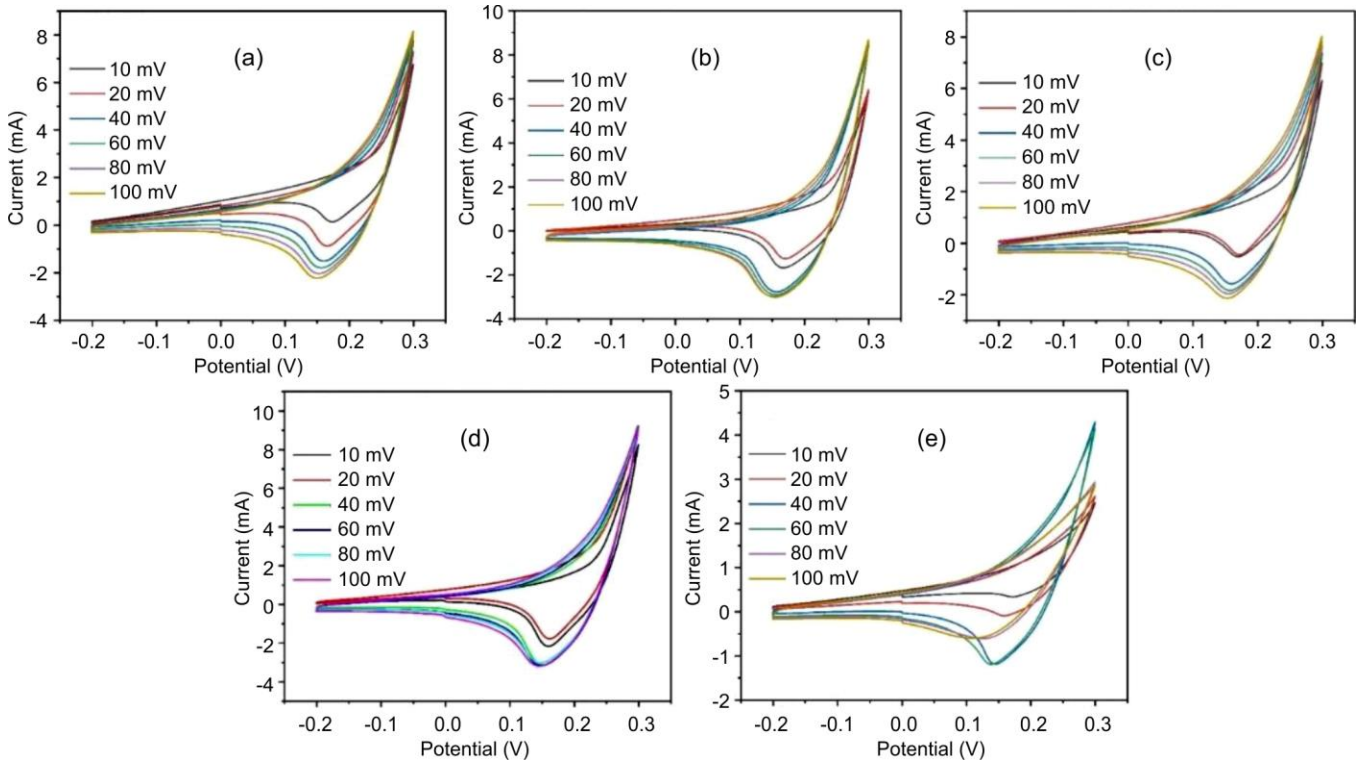

Fig. 5. CV graphs of (a) $Fe_2(MoO_4)_3$, (b) $Fe_2(MoO_4)_3$:1.0 g g-C_3N_4, (c) $Fe_2(MoO_4)_3$:1.5 g g-C_3N_4, (d) $Fe_2(MoO_4)_3$:2.0 g g-C_3N_4 and (e) g-C_3N_4

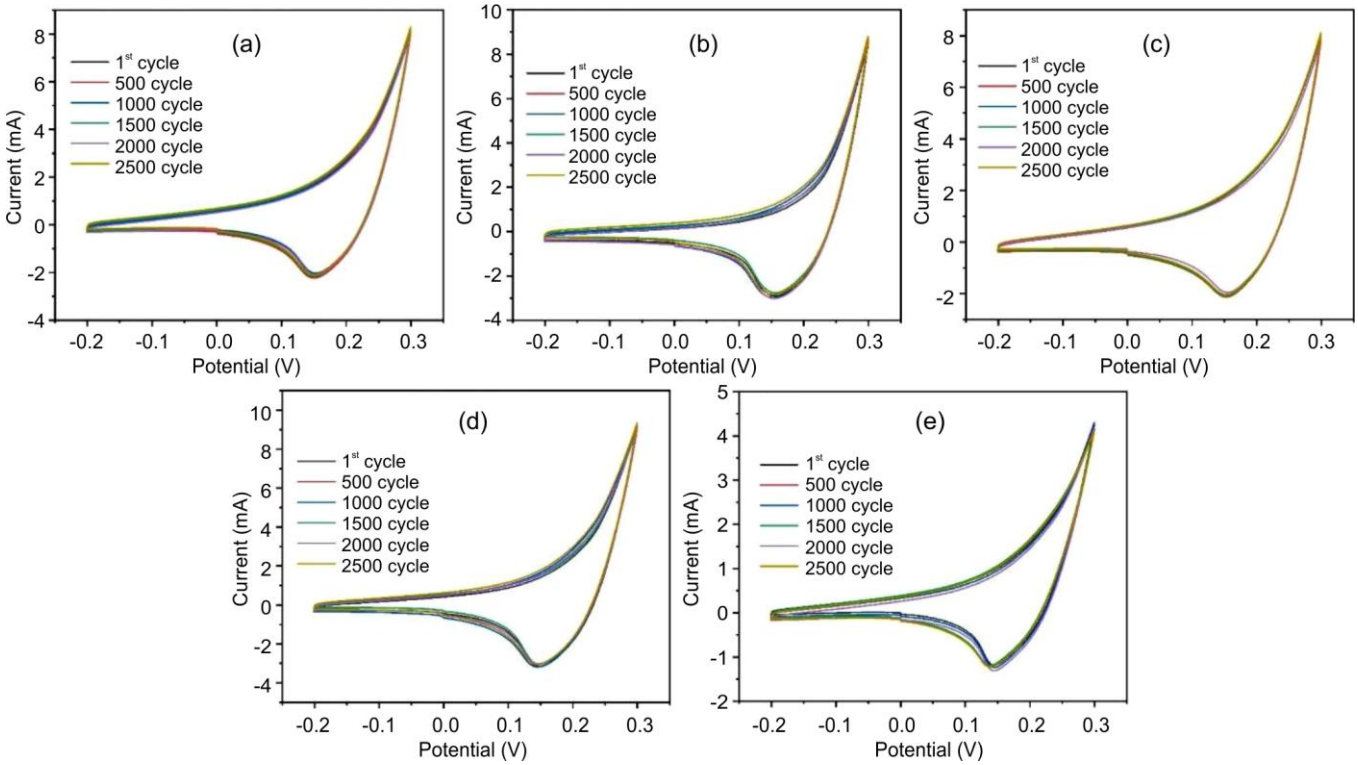

Fig. 6. CV cyclic stability graphs of (a) $Fe_2(MoO_4)_3$, (b) $Fe_2(MoO_4)_3$:1.0 g *g*-C_3N_4, (c) $Fe_2(MoO_4)_3$:1.5 g *g*-C_3N_4, (d) $Fe_2(MoO_4)_3$:2.0 g *g*-C_3N_4 and (e) *g*-C_3N_4

voltammetry (CV) tests for up to 2500 cycles at a scan rate of 100 mV/s, as displayed in Fig. 6a-e. This approach is well-established in the literature for assessing electrochemical performance and durability; for instance, CV cycling at consistent scan rates is frequently utilized to quantify both capacitance retention and charge-storage capability in novel supercapacitor electrodes, supporting their long-term cycling stability and material robustness under repeated electrochemical stress.

Fig. 7 visually summarizes the cyclic voltammetry results for cyclic stability and specific capacitance, while Table-2 details the corresponding specific capacitance values and retention rates achieved for optimized $Fe_2(MoO_4)_3$:*g*-C_3N_4 composites. The unmodified *g*-C_3N_4 electrode achieved a specific capacitance of 521.22 F/g and retained 98.24% of its capacity following extended cycling. In comparison, the $Fe_2(MoO_4)_3$ electrode exhibited a substantially greater specific capacitance of 954.65 F/g as well as a superior retention rate of 99.45%, underscoring its promise for robust and high-performance supercapacitor applications. These results reflect the significant impact of transition metal-based materials like $Fe_2(MoO_4)_3$ in enhancing charge storage capacity and cycling durability relative to typical carbon nitride-based electrodes. Upon introducing *g*-C_3N_4 as dopant into $Fe_2(MoO_4)_3$, a synergistic enhancement was observed: the $Fe_2(MoO_4)_3$:1*g*-C_3N_4 composite achieved 966.72 F/g with a retention rate of 99.52%. Further increasing the *g*-C_3N_4 loading to 1.5 g and 2 g elevated the specific capacitance to 993.75 F/g and 1157.16 F/g and the retention rates to 99.64% and 99.70%, respectively. These data collectively confirm that the strategic inclusion of *g*-C_3N_4 into the $Fe_2(MoO_4)_3$ matrix significantly improves both charge storage capacity and cyclic durability, a finding well aligned

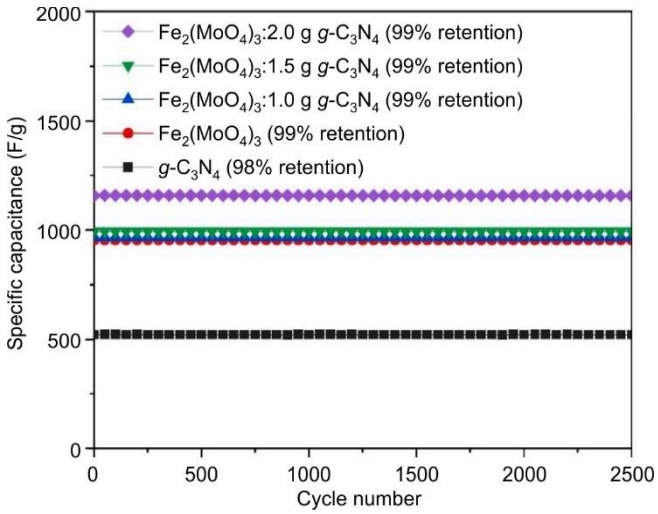

Fig. 7. CV cyclic stability and specific capacitance

TABLE-2
SPECIFIC CAPACITANCE AND RETENTION RESULTS OF OPTIMIZED $Fe_2(MoO_4)_3$:*g*-C_3N_4

Sample	Specific capacitance ($F\ g^{-1}$)	Retention (%)
g-C_3N_4	521.22	98.24
$Fe_2(MoO_4)_3$	954.65	99.45
$Fe_2(MoO_4)_3$:1.0 g *g*-C_3N_4	966.72	99.52
$Fe_2(MoO_4)_3$:1.5 g *g*-C_3N_4	993.75	99.64
$Fe_2(MoO_4)_3$:2.0 g *g*-C_3N_4	1157.16	99.70

with other studies demonstrating the positive role of *g*-C_3N_4 in composite supercapacitor performance [5,8,24].

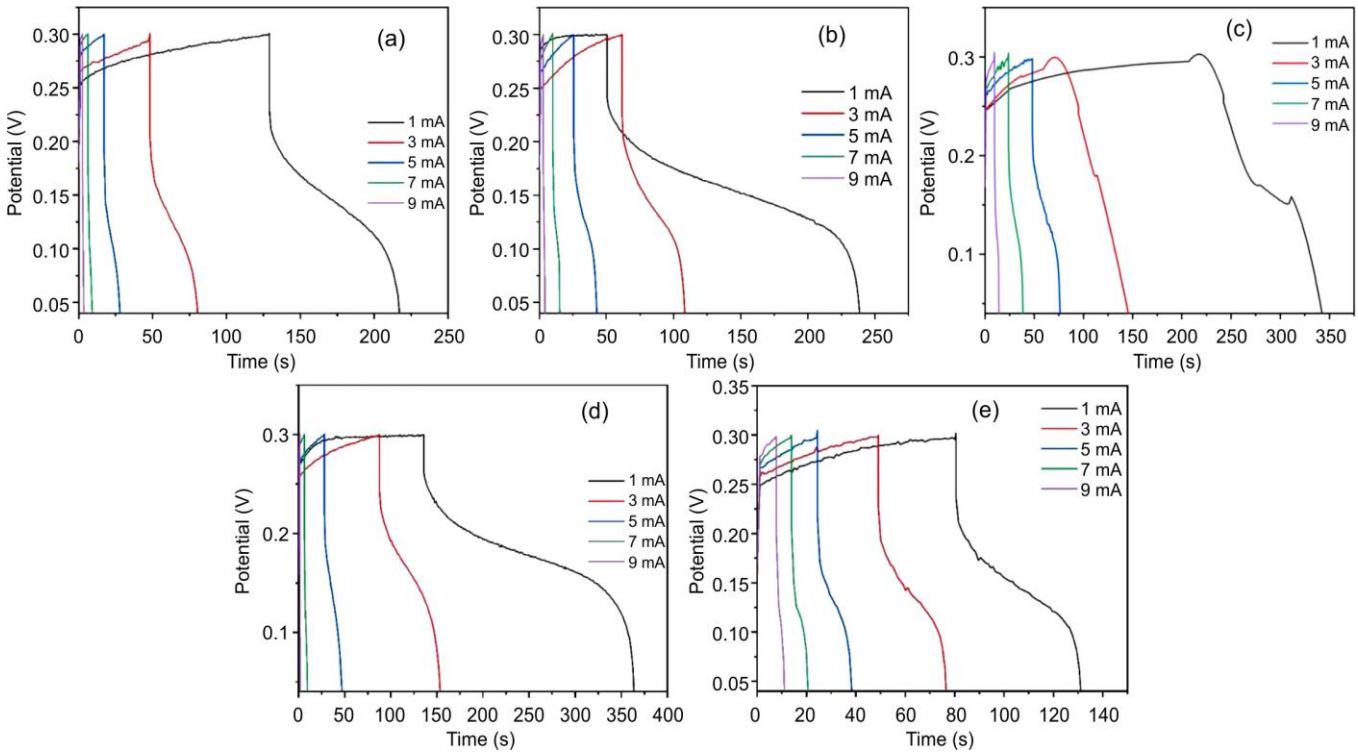

Fig. 8. GCD graphs of (a) $Fe_2(MoO_4)_3$, (b) $Fe_2(MoO_4)_3$:1 g *g*-C_3N_4, (c) $Fe_2(MoO_4)_3$:1.5 g *g*-C_3N_4, (d) $Fe_2(MoO_4)_3$:2 g *g*-C_3N_4 and (e) *g*-C_3N_4

GCD measurements: To assess the capacitive performance of the electrode materials, galvanostatic charge-discharge (GCD) measurements were systematically carried out at multiple current densities (1, 3, 5, 7 and 9 mA) within the voltage range of 0.0 to 0.3 V, as illustrated in Fig. 8a-d. This approach enabled the detailed examination of charge storage characteristics and rate capability under varying operational conditions. The non-linear shapes of the charge curves in all cases were mainly due to the IR (internal resistance) drop, resulting from the internal resistance of electrode and the resistance of solvent [25-28]. The galvanostatic charge-discharge profiles for $Fe_2(MoO_4)_3$ and its *g*-C_3N_4 hybrids (across 1-2 g *g*-C_3N_4 loadings) exhibit excellent symmetry, which is a hallmark of outstanding capacitive performance and highly reversible redox processes in supercapacitor electrodes. Importantly, a higher proportion of *g*-C_3N_4 leads to further improvements in pseudocapacitive characteristics, owing to the material's nanostructure offering more accessible redox-active sites and facilitating rapid ion/electron transfer at the electrode interface. This observation aligns with contemporary insights on the impact of nanocomposite design for advanced energy storage, where the synergy between Fe-based oxides and carbon nitride modulates the kinetics and interfacial charge storage, thereby maximizing electrochemical output.

Electrochemical impedance (EIS) analysis: Electrochemical impedance spectroscopy (EIS) measurements provide valuable insights into both ion transport and the electrical conductivity of electrode materials, enabling the decomposition of various resistive and capacitive elements within complex systems [6,8,10]. In this investigation, five electrode configurations including *g*-C_3N_4, pristine $Fe_2(MoO_4)_3$ and $Fe_2(MoO_4)_3$: *g*-C_3N_4 composites with 1, 1.5 and 2 g additions were systematically assessed using Nyquist plot analysis, as shown in Fig. 9. The resulting impedance spectra are characterized by a prominent semicircle in the high-frequency domain, which reflects the interfacial charge-transfer resistance at the electrode-electrolyte boundary and a linear tail at lower frequencies, indicative of efficient ion transport and pronounced capacitive behaviour [12,13]. A reduction in the diameter of the high-frequency semicircle signifies diminished charge-transfer resistance, directly correlating with increased electrical conductivity within the electrode network [5,13]. The high-frequency interception on the real axis denotes the equivalent series resistance, capturing the collective influence of the electrolyte,

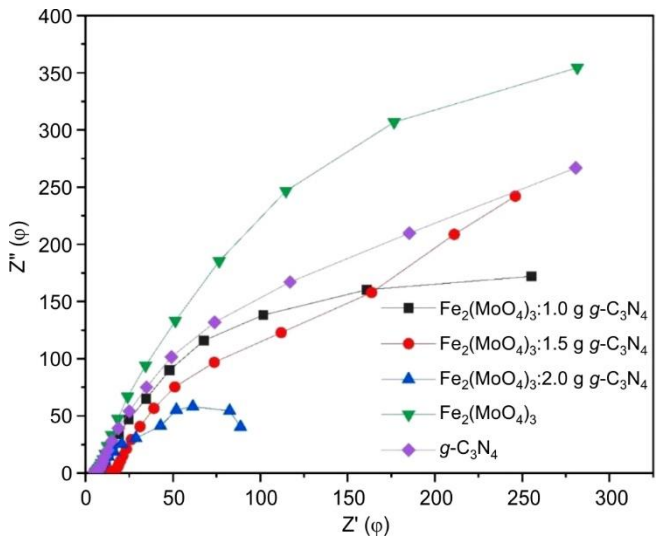

Fig. 9. Electrochemical impedance spectra of $Fe_2(MoO_4)_3$ and $Fe_2(MoO_4)_3$: *g*-C_3N_4

intra-grain resistance and interfacial contact resistance with current collectors [12,18]. In the low-frequency region, the emergence of a steep linear tail is associated with superior ionic mobility and efficient pseudocapacitive charge storage processes, effects that are especially amplified in $Fe_2(MoO_4)_3$: *g*-C_3N_4 hybrid electrodes with optimized *g*-C_3N_4 loading [7,9,10]. These EIS results collectively confirm that the incorporation of *g*-C_3N_4 enhances the pseudocapacitive behaviour and overall electrochemical performance of $Fe_2(MoO_4)_3$ based electrodes, aligning with the advanced design strategies for nanostructured composites in supercapacitor applications [5,7].

Conclusion

In conclusion, the hydrothermal synthesis route proved effective for the preparation of both pure and *g*-C_3N_4-modified $Fe_2(MoO_4)_3$. XRD patterns of the synthesized materials showed that each exhibited a single-phase orthorhombic structure assigned to the *Pbcn* space group, with the parent $Fe_2(MoO_4)_3$ phase remaining predominant even after modification with *g*-C_3N_4. This finding affirms that the orthorhombic lattice framework accommodates the presence of *g*-C_3N_4 without loss of crystallinity or phase homogeneity. Morphological analysis using FESEM and compositional confirmation *via* EDS verified the elemental purity of the samples. The FTIR spectroscopy proved the formation of $Fe_2(MoO_4)_3$ through bands located within the 800-500 cm^{-1} region. The electrochemical tests on $Fe_2(MoO_4)_3$ doped with 2 g of *g*-C_3N_4 revealed outstanding performance through analysis of cyclic voltammetry (CV), which provide a specific capacitance of 1157.16 F g^{-1} under conditions of 1 M KOH electrolyte tests. The tested material showed the superior cyclic performance since it maintained 99.70% of its highest capacitance after conducting 2500 charge-discharge cycles. The results confirm that *g*-C_3N_4-doped $Fe_2(MoO_4)_3$ shows outstanding potential to function as an advanced electrochemical electrode material.

ACKNOWLEDGEMENTS

This study was supported by the Government Arts College, Coimbatore, and the authors are also grateful to the Government College of Technology for providing the necessary materials.

CONFLICT OF INTEREST

The authors declare that there is no conflict of interests regarding the publication of this article.

REFERENCES

1. D. Zhang, X. Zhang, Y. Chen, C. Wang, Y. Ma, H. Dong, L. Jiang, Q. Meng and W. Hu, *Phys. Chem. Chem. Phys.*, **14**, 10899 (2012); https://doi.org/10.1039/C2CP41051F
2. A. Patel, S. K. Patel, R. S. Singh and R.P. Patel, *Discover Nano*, **19**, 188 (2024); https://doi.org/10.1186/s11671-024-04053-1
3. M. Neelakandan, P. Dhandapani, S. Ramasamy, R. Duraisamy, S.J. Lee and S. Angaiah, *RSC Adv.*, **15**, 16766 (2025); https://doi.org/10.1039/D5RA01950H
4. C. Cheng and G. Lai, *Mater. Lett.*, **301**, 130246 (2021); https://doi.org/10.1016/j.matlet.2021.130246
5. S.K. Ghosh, *ACS Omega*, **40**, 25493 (2020); https://doi.org/10.1021/acsomega.0c03455
6. H.T. Huu and W.B. Im, *ACS Appl. Mater. Interfaces*, **12**, 35152 (2020); https://doi.org/10.1021/acsami.0c11862
7. B. Hu, S. Jian, G. Yin, W. Feng, Y. Cao, J. Bai, Y. Lai, H. Tan, and Y. Dong, *Nanomaterials*, **11**, 3302 (2021); https://doi.org/10.3390/nano11123302
8. M. Gowtham, N.S. Kumar, C. Sivakumar and K. Mohanraj, *NanoNEXT*, **3**, 1 (2022); https://doi.org/10.54392/nnxt2221
9. Y. Kimura, S. Kobayashi, S. Kawaguchi, K. Ohara, Y. Suzuki, T. Nakamura, Y. Iriyama, and K. Amezawa, *RSC Adv.*, **14**, 18109 (2024); https://doi.org/10.1039/d4ra03058c
10. D.K. Ponelakkia, V. Balaji, K. Muhil Eswari, R.M. Nivetha, R. Yuvakkumar and G. Ravi, *Mater. Lett.*, **363**, 136269 (2024); https://doi.org/10.1016/j.matlet.2024.136269
11. Q. Yang, Z. Hu, A. Yang and Y.F. Yuan, *J. Electron. Mater.*, **54**, 1029 (2025); https://doi.org/10.1007/s11664-024-11619-3
12. X. Chang, X. Zhai, S. Sun, D. Gu, L. Dong, Y. Yin and Y. Zhu, *Nanotechnology*, **28**, 135705 (2017); https://doi.org/10.1088/1361-6528/aa6107
13. M.M. Taha, L.G. Ghanem, M.A. Hamza and N.K. Allam, *ACS Appl. Energy Mater.*, **4**, 10344 (2021); https://doi.org/10.1021/acsaem.1c02280
14. S. Vinoth, K. Subramani, W.J. Ong, M. Sathish and A. Pandikumar, *J. Colloid Interface Sci.*, **584**, 204 (2021); https://doi.org/10.1016/j.jcis.2020.09.071
15. M.G. da Silva Júnior, L.C.C. Arzuza, H.B. Sales, R.M. da C. Farias, G. de A. Neves, H. de L. Lira and R.R. Menezes, *Materials*, **16**, 7657 (2023); https://doi.org/10.3390/ma16247657
16. S. Parveen, I.A. Bhatti, A. Ashar, T. Javed, M. Mohsin, M.T. Hussain, M.I. Khan, S. Naz and M. Iqbal, *Mater. Res. Express*, **7**, 035016 (2020); https://doi.org/10.1088/2053-1591/ab73fa
17. K. Thiagarajan, T. Bavani, P. Arunachalam, S.J. Lee, J. Theerthagiri, J. Madhavan, B.G. Pollet and M.Y. Choi, *Nanomaterials*, **10**, 392 (2020); https://doi.org/10.3390/nano10020392
18. L. Ge, C. Han, J. Liu and Y. Li, *Appl. Catal. A Gen.*, **409-410**, 215 (2011); https://doi.org/10.1016/j.apcata.2011.10.006
19. U. Kersen and R.L. Keiski, *Catal. Commun.*, **10**, 1039 (2009); https://doi.org/10.1016/j.catcom.2008.12.052
20. H. Oudghiri-Hassani, *Catal. Commun.*, **60**, 19 (2015); https://doi.org/10.1016/j.catcom.2014.11.019
21. A. Mohmoud, S. Rakass, H. Oudghiri Hassani, F. Kooli, M. Abboudi and S. Ben Aoun, *Molecules*, **25**, 5100 (2020); https://doi.org/10.3390/molecules25215100
22. K. Seevakan, A. Manikandan, P. Devendran, S.A. Antony and T.J.A.S. Alagesan, *Adv. Sci. Eng. Med.*, **8**, 566 (2016); https://doi.org/10.1166/asem.2016.1884
23. A. Dutta, S. Adhikari, P. Johari, R. Nag, A. Bera, S.K. Saha and A.J. Akhtar, *J. Energy Storage*, **85**, 111082 (2024); https://doi.org/10.1016/j.est.2024.111082
24. Y. Su, S. Chen, Q. Yang and Y. Wang, *Chem. Eng. Sci.*, **217**, 115517 (2020); https://doi.org/10.1016/j.ces.2020.115517
25. H. Liang, H. Zhang, L. Zhao, Z. Chen, C. Huang, C. Zhang, Z. Liang, Y. Wang, X. Wang, Q. Li, X. Guo and H. Li, *Chem. Eng. J.*, **427**, 131481 (2022); https://doi.org/10.1016/j.cej.2021.131481
26. H.T. Huu, N.S.M. Viswanath, N.H. Vu, J.W. Lee and W.B. Im, *Nano Res.*, **14**, 3977 (2021); https://doi.org/10.1007/s12274-021-3323-1
27. M. Seethalakshmi, D.M. Shanthi, S. Dhanapandian and D.K. Ashokkumar, *Asian J. Chem.*, **37**, 39 (2024); https://doi.org/10.14233/ajchem.2025.32787
28. T. Chen, C. Xiang, Y. Zou, F. Xu and L. Sun, *Energy Fuels*, **35**, 10250 (2021); https://doi.org/10.1021/acs.energyfuels.1c00913